RSC Advances



PAPER

View Article Online

View Journal | View Issue



Cite this: RSC Adv., 2019, 9, 38952

Formation of sulfur trioxide during the SCR of NO with NH_3 over a V_2O_5/TiO_2 catalyst

Jin Xiong, Dab Yuran Li,*a Yuting Lina and Tingyu Zhu*ac

The oxidation of sulfur dioxide (SO_2) to sulfur trioxide (SO_3) is an undesirable reaction that occurs during the selective catalytic reduction (SCR) of nitrogen oxides (NO_x) with ammonia (NH₃), which is a process applied to purify flue gas from coal-fired power plants. The objectives of this work were to establish the fundamental kinetics of SO_3 formation over a V_2O_5/TiO_2 catalyst and to illustrate the formation mechanism of SO₃ in the presence of NO_x, H₂O and NH₃. A fixed-bed reactor was combined with a Fourier transform infrared (FTIR) spectrometer and a Pentol SO₃ analyser to test the outlet concentrations of the multiple components. The results showed that the rate of SO2 oxidation was zeroorder in O_2 , 0.77-order in SO_2 and -0.19-order in SO_3 and that the apparent activation energy for SO_2 oxidation was 74.3 kJ mol⁻¹ over the range of studied conditions. Based on in situ diffuse reflectance infrared Fourier transform (in situ DRIFT) spectroscopy, X-ray photoelectron spectroscopy (XPS) and temperature programmed desorption (TPD) tests, the SO₃ formation process is described here in detail. The adsorbed SO₂ was oxidized by V₂O₅ to produce adsorbed SO₃ in the form of bridge tridentate sulfate, and the adsorbed SO_3 was desorbed to the gas phase. NO_x promoted the oxidation of the adsorbed SO₂ due to the promotion of the conversion of low-valent vanadium to high-valent vanadium. In addition, the desorption of the adsorbed SO₃ was inhibited by H₂O or NH₃ due to the conversion of tridentate sulfate to the more stable bidentate sulfate or ammonium bisulfate. Finally, the mechanism of the influence of NO_v, H₂O and NH₃ on the formation of gaseous SO₃ was proposed.

Received 9th October 2019 Accepted 18th November 2019

DOI: 10.1039/c9ra08191g

rsc.li/rsc-advances

1. Introduction

As the use of equipment for the selective catalytic reduction (SCR) of NO_x has increased in recent years, the emission of SO₃ in coal-fired power plants has attracted more attention. 1-3 SO₃ increases the acid dew point of flue gas, and sulfuric acid forms when the flue gas is cooled, which corrodes the downstream equipment and pipelines. 4,5 When the SO₃ concentration in flue gas is more than 5 ppm (18 mg m⁻³), an opaque plume is generated, and a "blue acid plume" appears in the downwind direction of the chimney. 6-9 To solve the problem of SO₃ pollution, strict emission standards have been established.6 In the United States, 22 states have proposed SO₃ emission limits for coal-fired flue gas, of which 14 states have a limit of 6 mg m⁻³. The SO₃ emission limits in Singapore are 10 mg m⁻³ for flue gas from stationary sources. The daily SO2 and SO3 emission limits in Germany are 50 mg m⁻³. In China, regulations have been issued for "eliminating the white smoke" from

industrial flue gas, aiming to expose the "blue" and "yellow" smoke from SO₃ and NO₂, respectively, to achieve deep purification of the smoke. ^{10,11} Therefore, research on the SO₃ formation process is very important and urgent.

There has been much discussion about the process of SO₂ oxidation to SO_3 on a V_2O_5/TiO_2 catalyst. Dunn J. P. $^{12-15}$ studied the oxidation ability of several binary catalysts for SO2 and found that the oxidation ability of V₂O₅ is greater than that of other transition metal oxides. In addition, the oxidation mechanism of SO₂ on a V₂O₅/TiO₂ catalyst has been proposed. SO₂ may adsorb and coordinate onto the vanadium-oxygensupport (V–O–M) bond, resulting in the $(V^{5+}) \cdot SO_{2-ads}$ state. This process is followed by the cleavage of the V5+-O-SO2 and formation of gaseous SO3, which represents the rate determining step. The preferential adsorption of SO₃ results in stronger bonding of SO₃ to the surface vanadium species and competitive adsorption of SO₂ on the active sites. In contrast, Guo X. et al. studied the sulfate species on a V₂O₅/TiO₂ catalyst and concluded that sulfate species are formed on titanium instead of vanadium.16

 $\rm H_2O$ and $\rm NH_3$ in the atmosphere can inhibit the oxidation of $\rm SO_2$ to $\rm SO_3$, while $\rm NO_x$ has a promotive influence. ^{7,17–22} However, the mechanisms of these effects have not been described in detail. Kinetics research is of great significance for revealing the reaction mechanism, evaluating the influence of various factors

Beijing Engineering Research Center of Process Pollution Control, National Engineering Laboratory for Hydrometallurgical Cleaner Production Technology, Institute of Process Engineering, Chinese Academy of Sciences, Beijing 100190, China. E-mail: yrli@ipe.ac.cn; tyzhu@ipe.ac.cn

^bUniversity of Chinese Academy of Sciences, Beijing 100049, China

Center for Excellence in Regional Atmospheric Environment, Institute of Urban Environment, Chinese Academy of Sciences, Xiamen 361021, China

and guiding appropriate process design. However, kinetic research on the oxidation process of SO_2 is limited. Therefore, it is necessary to simulate the process and influencing factors of SO_2 oxidation over the V_2O_5/TiO_2 catalyst. In this work, the effects of O_2 and SO_2 on SO_3 formation were studied, and the reaction order with respect to the reactants and the apparent activation energy during SO_2 oxidation were calculated to establish the basic kinetics of SO_2 oxidation on a V_2O_5/TiO_2 catalyst. Then, a proposed formation mechanism of SO_3 in a complex atmosphere was obtained by studying the effects of H_2O_1 , NO_2 and NH_3 on the SO_3 formation process.

2. Experimental

Paper

2.1. Catalyst preparation and characterization

The 5 wt% V_2O_5/TiO_2 catalysts were prepared by the wet impregnation method. Commercial P25 TiO_2 was calcined at 450 °C for 4 h. NH₄VO₃, the precursor for V_2O_5 , was dissolved in distilled water at 80 °C; P25 TiO_2 was added into the NH₄VO₃ solution, and then the solution was stirred for 1 h and subsequently dried by a rotary evaporator. The obtained powder was calcined in air at 450 °C for 4 h and pulverized to a size of 180–250 μ m.

The pore properties of the P25-TiO₂ and V_2O_5/TiO_2 catalysts were determined at 77 K through N₂ adsorption (NOVA3200e, Quantachrome, USA). The Brunauer–Emmett–Teller (BET) surface area ($S_{\rm BET}$) and the average pore diameter (d) were calculated by the BET method and Horvath–Kawazoe equation method, respectively. The total pore volume (V_t) was calculated directly. The results are shown in Table 1. The carrier and catalyst both displayed a mesoporous structure.

Powder X-ray diffraction (XRD, Empyrean, PANalytical B.V., Netherlands) patterns were recorded on a diffractometer (Rigaku D/Max-RA) at 40 kV and 150 mA employing Cu K_{α} radiation, and the results are shown in Fig. 1. The XRD patterns of the catalyst exhibited a mixed phase of anatase (PDF #21-1272) and rutile (PDF #21-1276) TiO₂. The diffraction peaks of V_2O_5 (PDF #41-1426) at 15.4°, 20.4°, 21.7°, 26.2° and 31.0° were not observed, indicating that the V_2O_5 was well distributed on the carrier, with no agglomerated microcrystals for the $V_2O_5/$ TiO₂ catalyst.

X-ray photoelectron spectroscopy (XPS) was used to characterize the vanadium on the catalyst surface using a hemispherical energy analyser (ESCALAB 250Xi, Thermo Fisher, USA). The main C 1s peak at 284.6 eV was used as an internal standard to calibrate the binding energies. The areas of the main peaks for V $2p_{3/2}$ were detected, and the Gaussian–Lorentzian deconvolution method was utilized to calculate the vanadium contents of the various valences.

Table 1 Pore properties of the carrier and catalyst

Sample	$S_{\mathrm{BET}} \left(\mathrm{m}^2 \mathrm{g}^{-1}\right)$	$V_{\rm t} ({ m ml g}^{-1})$	d (nm)	
$\begin{array}{c} \text{P25-TiO}_2\\ \text{V}_2\text{O}_5/\text{TiO}_2 \end{array}$	55	0.262	19.14	
	50	0.258	20.96	

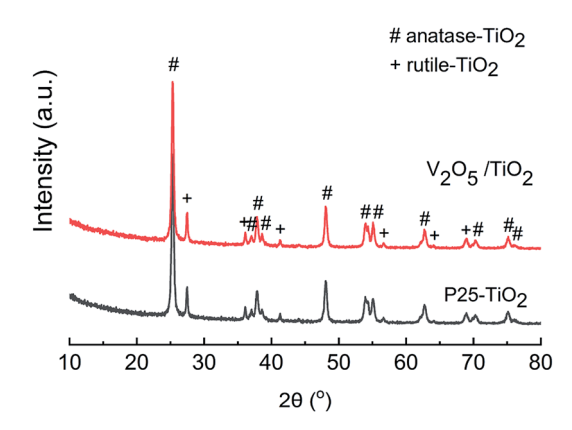


Fig. 1 XRD patterns of the carrier and catalyst.

In situ diffuse reflectance infrared Fourier transform (*in situ* DRIFT) spectra were collected on a Fourier transform infrared (FTIR) spectrometer (Tensor 27, Bruker, Germany) to investigate the oxidation of SO₂. The spectra were obtained by averaging 16 scans with a resolution of 2 cm⁻¹.

2.2. Activity measurement

The oxidation reactions of SO_2 to generate SO_3 were investigated in a quartz reactor with both an on-line FTIR spectrometer (Tensor 27, Bruker, Germany) capable of quantifying SO_2 with an error of 1% and an on-line SO_3 analyser (Pentol GmbH, Germany) capable of quantifying SO_3 with an error of 10%, 23 as shown in Fig. 2. The gas flow rate for the standard state was 300 ml min $^{-1}$ with an error of 1%. The gaseous hourly space velocity (GHSV) was approximately 19 000 h $^{-1}$.

The default reaction conditions for the SO_2 oxidation included 320 °C, 1000 ppm SO_2 , 6 vol% O_2 , and N_2 balance. When appropriate, 500 ppm NO_x (NO accounted for approximately 90%, and the remainder was NO_2), 500 ppm NH_3 , or 5 vol% H_2O was introduced to the mixture gas. The reaction temperature ranged from 180 °C to 400 °C with an error of 0.1 °C. The SO_2 concentration varied between 500 and 1500 ppm, and the O_2 concentration ranged from 0.1 vol% to 10 vol%. In various sections of this work, the different components of the mixture gas were evaluated and are shown in Table 2.

Water vapor was prepared according to the saturation method (ISO 6145-9: 2009, IDT). As shown in orange in Fig. 2, the pipelines through which the water vapor flowed were insulated and maintained at 80–90 °C. Note that the NH $_3$ had a significant impact on the measurement of SO $_3$, so the NH $_3$ was turned off after a relatively short time, before it penetrated the catalyst, to reduce its influence on SO $_3$ detection. Assuming standard operating conditions, the SO $_2$ and O $_2$ gas diffusivities were calculated, and then the effectiveness factors were calculated to be 0.99–1.00 for the catalyst particle sizes tested from 150 to 550 μ m, indicating that internal diffusion could be neglected. When the gas speed in a vacant tube is above 9.6 cm s $^{-1}$, the impact of external diffusion on the SO $_2$ conversion can be ignored. In this work, a catalyst particle size of 180–250 μ m

RSC Advances Paper

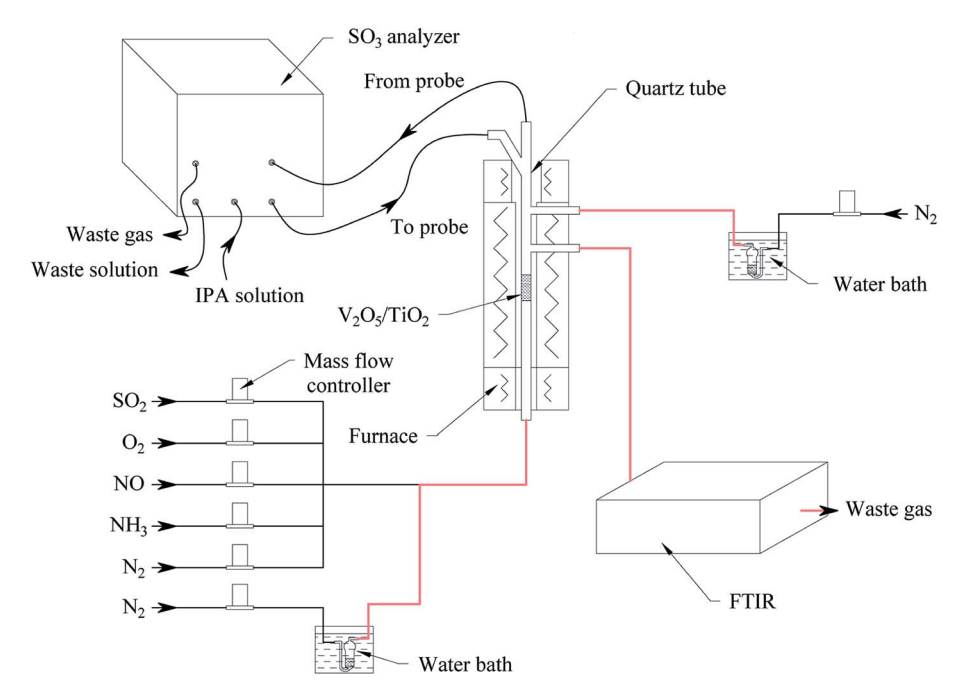


Fig. 2 The schematic diagram of the activity measurement.

Table 2 Components of the mixture gas for various testing purposes

Section	Components of the mixture gas		
3.1, 3.2	SO ₂ , O ₂ and N ₂		
3.3, 3.4	SO_2 , O_2 and N_2 ; NO_x , NH_3 or H_2O (if used)		
3.5	SO_2 and N_2 ; O_2 , NO_x , NH_3 or H_2O (if used)		

was selected, and the gas speed in the vacant tube was maintained at $10.6~{\rm cm~s}^{-1}$; thus, the effects of internal diffusion and external diffusion were eliminated.

For the temperature-programmed desorption (TPD) experiments, the V_2O_5/TiO_2 catalyst was first processed in a 1000 ppm SO_2 and 6 vol% O_2 atmosphere at 320 °C for 180 min and then processed in a N_2 , 5 vol% H_2O or 500 ppm NH_3 atmosphere, respectively, for 20 min. Finally, the TPD tests were carried out

in N_2 with a heating rate of 5 $^{\circ}\text{C min}^{-1}$ until the temperature reached 800 $^{\circ}\text{C}.$

3. Results and discussion

3.1. Reaction order and apparent activation energy

To determine the reaction order of SO_2 oxidation to SO_3 at various temperatures, the effect of the O_2 and SO_2 concentrations on SO_3 generation was evaluated, as shown in Fig. 3. In Fig. 3(a), even when the O_2 concentration was zero, some SO_3 was produced at various temperatures, indicating that the oxygen atom in V_2O_5 participated in the oxidation of SO_2 . This result was consistent with the Mars-van-Krevelen (M–K) mechanism, in which the first step involves reduction of the oxygen vacancy produced by the reactants and catalysts and the second step involves replacement of the oxygen vacancies with oxygen adsorbed by dissociation.²⁴ With increasing O_2 concentration,

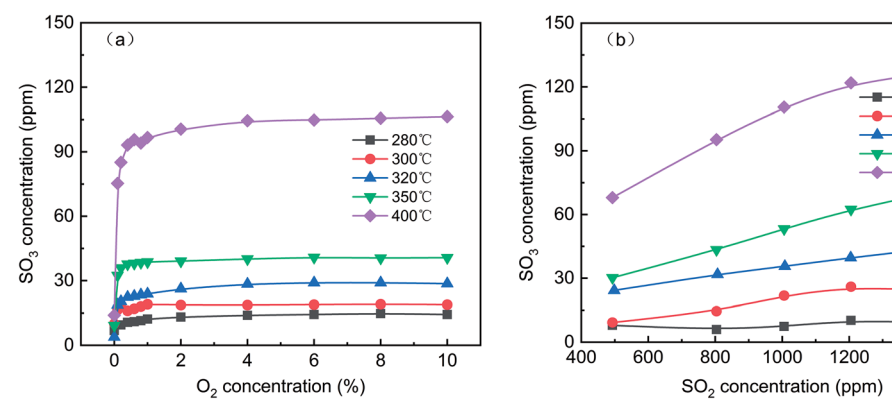


Fig. 3 Effect of the O₂ (a) and SO₂ (b) concentrations on SO₃ generation (default conditions: 1000 ppm SO₂, 6 vol% O₂, and N₂).

300°C 320°C

350℃

1400

Paper RSC Advances

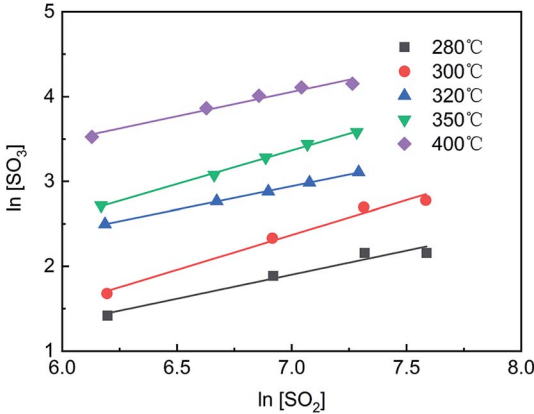


Fig. 4 $ln[SO_2]-ln[SO_3]$ at various temperatures.

the SO_3 concentration continued to increase, but the growth rate slowed until the O_2 concentration reached 1%. Thus, the reaction order was approximately zero when the O_2 concentration was more than 1%. Although the oxidation of SO_2 is an exothermic reaction, the increase in temperature was conducive to the formation of SO_3 because the reaction was far from the equilibrium. As shown in Fig. 3(b), as the SO_2 concentration increased from 500 ppm to 1500 ppm, the SO_3 concentration increased from 7.9 ppm to 9.0 ppm at 280 °C and from 68.0 ppm to 127.4 ppm at 400 °C. The SO_2 conversion quantity increased linearly with the SO_2 concentration, and the higher the temperature was, the greater the slope of the curve was.

The chemical equation for SO_2 oxidation is shown in eqn (1). The generalized reaction rate equation is shown in eqn (2), and the linearized form is shown in eqn (3). The oxidation rate of SO_2 was low in this experiment, so the following assumptions were made: (1) $r_{SO_2} = [SO_3]/\tau$, and the residence time (τ) is a constant; and (2) $[SO_2]$ and $[SO_3]$ are the averages of their import and export concentrations. The reaction order in O_2 was approximately zero. Thus, eqn (3) can be further simplified to eqn (4).

$$2SO_2 + O_2 \leftrightarrow 2SO_3 \tag{1}$$

$$r_{SO_3} = k[SO_2]^a[SO_3]^b[O_2]^c \tag{2}$$

$$\ln r_{SO_2} = \ln k + a \ln[SO_2] + b \ln[SO_3] + c \ln[O_2]$$
 (3)

$$\ln[SO_3] = \frac{\ln k' + a \ln[SO_2]}{1 - b} \tag{4}$$

As shown in Fig. 4, the curves of $\ln[SO_2]$ versus $\ln[SO_3]$ were fitted using eqn (4), and a series of a and b values were obtained at various temperatures and are listed in Table 3. The average values of a and b were 0.77 \pm 0.05 and -0.19 \pm 0.08,

Table 3 Reaction orders (a, b) at various temperatures T (°C) 400 280 300 320 350 0.71 а 0.71 0.86 0.86 0.73 b -0.25-0.29-0.08-0.26-0.050.8895 0.9522 0.9993 0.9955 0.949

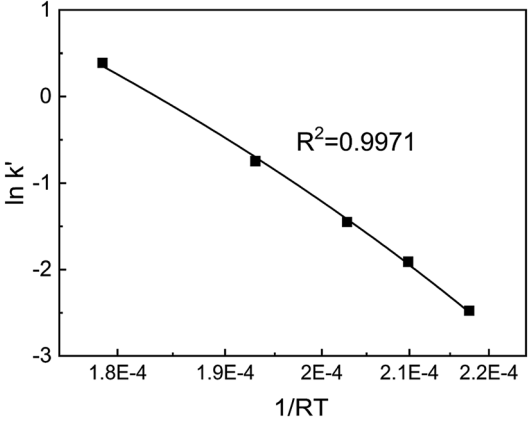


Fig. 5 Curve of 1/RT- $\ln k'$ for SO_2 oxidation.

respectively. The reaction rate equation of SO_2 over the V_2O_5 /TiO₂ catalyst is given by eqn (5).

$$r_{SO_2} = k'[SO_2]^{0.77}[SO_3]^{-0.19}$$
 (5)

Substituting the values of a and b into eqn (4) yields eqn (6). After a series of $\ln k'$ values at various temperatures was calculated by eqn (6), the resulting curve of 1/RT versus $\ln k'$ was obtained, as shown in Fig. 5. The slope of the curve was equal to the apparent activation energy, approximately 74.3 kJ mol^{-1} with an error of 2.4%. The reaction rate of SO_2 over the $\mathrm{V_2O_5}/\mathrm{TiO_2}$ catalyst is given by eqn (7).

$$\ln k' = 0.19 \ln[SO_3] - 0.77 \ln[SO_2]$$
 (6)

$$r_{SO_2} = Ae^{-\frac{74.3}{RT}}[SO_2]^{0.77}[SO_3]^{-0.19}$$
 (7)

The apparent activation energy of SO₂ oxidation was approximately 84–209 kJ mol⁻¹, so the chemical reaction was a rate-limiting step,²⁵ leading to both the shallow layer and deep layer of the catalyst being involved in the oxidation of SO₂. In contrast, the activation energy of the NO_x reduction reaction was small at approximately 21 kJ mol⁻¹,²⁶ and the chemical reaction rate was fast, resulting in only the shallow layer of the catalyst participating in the reduction of NO_x. According to the above differences, reducing the wall thickness of the catalyst was an effective method to reduce the oxidation rate of SO₂ while ensuring denitrification efficiency. In practice, the minimum thickness of the honeycomb walls is determined by their mechanical resistance.

3.2. Formation mechanism of SO₃

 SO_3 formation was first characterized in a simple atmosphere of SO_2 and O_2 , and then the effects of NO_x , H_2O and NH_3 on SO_3 formation were explored to further reveal the mechanism of SO_3 formation in complex atmospheres. *In situ* DRIFT spectra for the reaction in a simple atmosphere at various times are shown in Fig. 6. As the reaction proceeded, the stretching vibration of

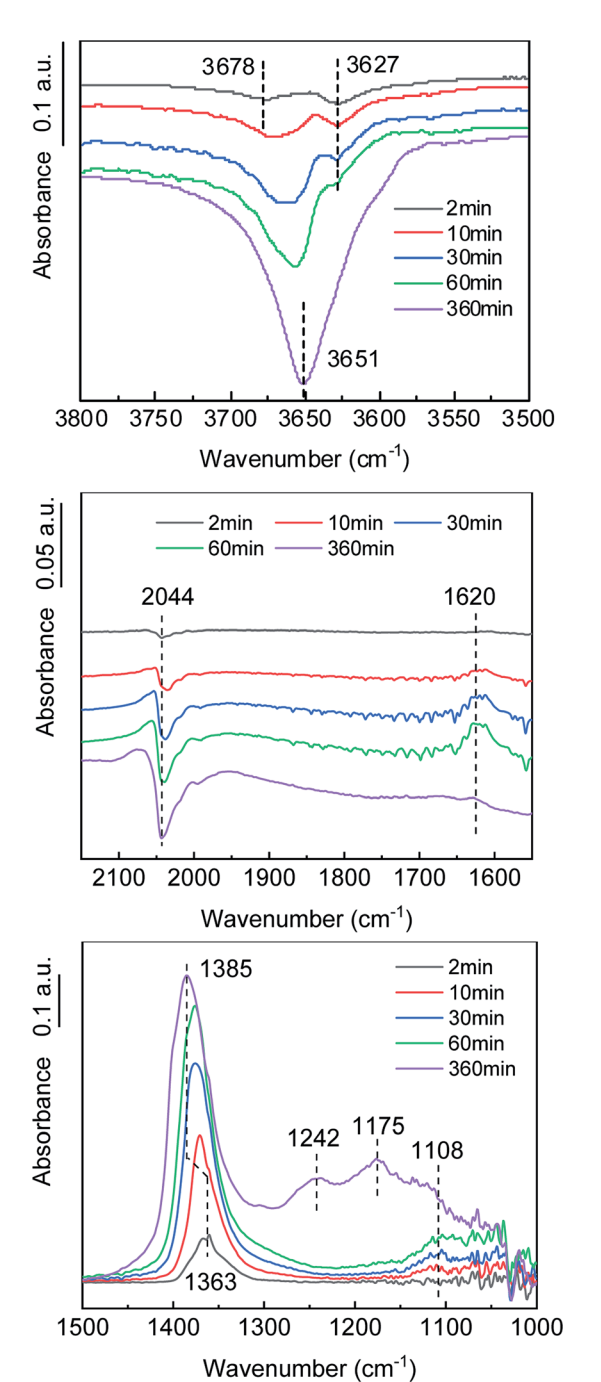


Fig. 6 In situ DRIFT spectra of the catalyst in the formation process of SO_3 . (Conditions: 1000 ppm SO_2 , 6 vol% O_2 , and N_2).

O–H at 3550–3750 cm⁻¹ decreased. The high frequency peak at 3678 cm⁻¹ was attributed to an alkaline hydroxyl group, and the low frequency peak at 3627 cm⁻¹ was attributed to a neutral hydroxyl group.²⁷ Based on the variation of the peak strength with reaction time, it was inferred that the alkaline hydroxyl groups were preferentially consumed. The peak at 1620 cm⁻¹ belonged to the H–O–H bending motion of adsorbed H₂O,²⁸ indicating that H₂O was formed during the adsorption of SO₂. The reduction of the surface hydroxyl group and the formation of adsorbed H₂O were a result of the SO₂ combining with the

surface hydroxyl group on the TiO_2 and releasing sulfite species and H_2O . The half peaks at $1030-1150~\text{cm}^{-1}$ indicated the existence of sulfite species on the catalyst surface.²⁸⁻³⁰

The vibration peak at 1363-1385 cm⁻¹ belonged to the bridge tridentate sulfate species bound to the carrier.16,31-33 As the reaction proceeded, the peak intensity increased, indicating that the surface sulfate increased. As the peak gradually shifted from 1363 cm⁻¹ to 1385 cm⁻¹, the hydroxyl peak gradually shifted from 3678 cm⁻¹ to 3651 cm⁻¹, which indicated that the bridge tridentate sulfate species was preferentially bound first to the basic hydroxyl group and then to the neutral hydroxyl group on the carrier. A comparison of the spectra at 60 min and 360 min revealed that the bending motion peak of H₂O disappeared, but the wide peak at 1100-1300 cm⁻¹ increased significantly. These peaks belonged to the chelated bidentate sulfate, bridge bidentate sulfate and unidentate sulfate.34 This observation indicated that the bridge tridentate sulfate changed to bidentate sulfate or unidentate sulfate under the action of H_2O .

The negative peak at $2044~\rm cm^{-1}$ belonged to the overtones of V=O.³⁵ The gradual deepening of the negative peak indicated that the ratio of the high-valent vanadium (V⁵⁺) was decreasing, which was consistent with the mechanism of the K-M reaction. As an active component, the V_2O_5 was reduced to low-valent vanadium (V³⁺) when the SO₂ was oxidized, and then the V³⁺ was oxidized to V⁵⁺ by O₂, thus completing a catalytic cycle. The formation process of gaseous SO₃, accompanied by the transformation between high-valent vanadium and low-valent vanadium, can be roughly divided into three steps. (1) Gaseous SO₂ is chemically adsorbed on the surface of the carrier through hydroxyl groups. (2) The chemically adsorbed SO₂ is oxidized by high-valent vanadium to form adsorbed SO₃. (3) The adsorbed SO₃ is desorbed to generate gaseous SO₃.

3.3. Effects of NO_x, H₂O and NH₃ on gaseous SO₃ formation

The effects of NO_x on SO_3 formation are shown in Fig. 7. With the addition of NO_x , the SO_3 concentration gradually increased from 11 ppm to 17.5 ppm and then remained constant, showing that NO_x promoted the generation of gaseous SO_3 by

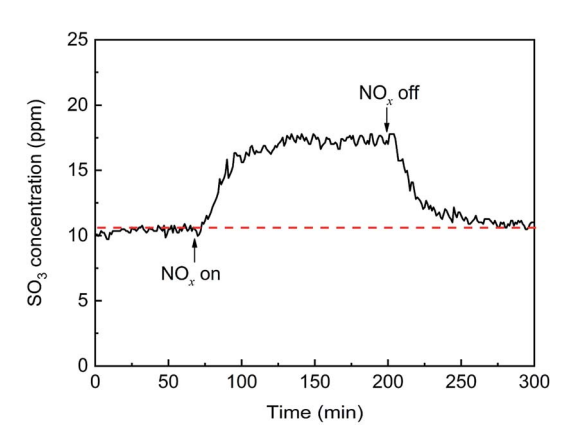


Fig. 7 Transient effects of NO_x on SO_3 formation (conditions: 1000 ppm SO_2 , 500 ppm NO_x , 6 vol (O_2) , and O_2).

Paper

25 (mdd) up 15 0 15 H₂O off H₂O on H₂O off Time (min)

Fig. 8 Transient effects of H_2O on SO_3 formation (conditions: 1000 ppm SO_2 , 5 vol% H_2O , 6 vol% O_2 , and N_2).

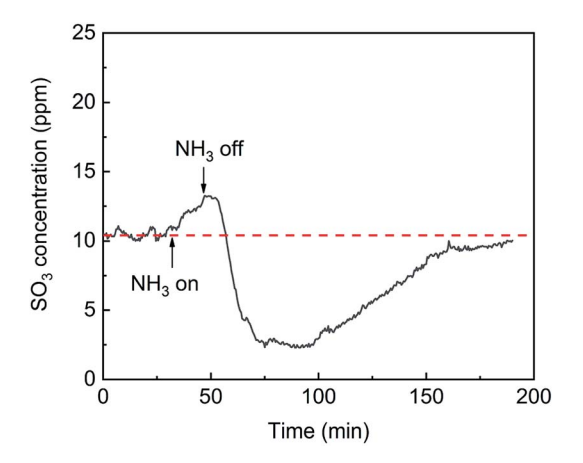


Fig. 9 Transient effects of NH_3 on SO_3 formation (conditions: 1000 ppm SO_2 , 500 ppm NH_3 , 6 vol (O_2, O_3) , and O_3).

approximately 60%. When the flow of NO_x was stopped, the SO_3 concentration gradually decreased to the initial concentration. The enhancement may have been due to the oxidation of SO_2 by NO_x , which was in the gas phase or adsorbed on the catalyst surface.

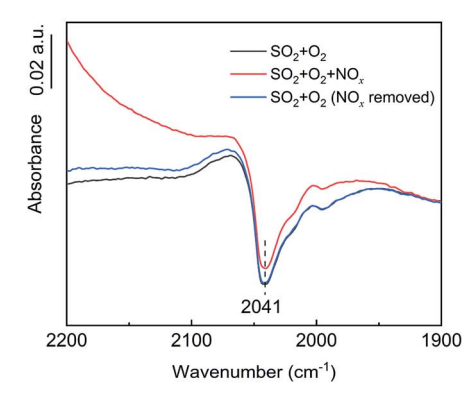
The effects of $\rm H_2O$ on $\rm SO_3$ formation are shown in Fig. 8. With the addition of $\rm H_2O$, the $\rm SO_3$ concentration sharply increased from 11 ppm to 23 ppm and then gradually decreased to 8.5 ppm. Compared with the initial concentration, the $\rm SO_3$ concentration first doubled and then decreased by 23%. It can be inferred that the $\rm SO_3$ desorption from the active site into the gas phase was due to a competitive adsorption between $\rm H_2O$ and $\rm SO_3$. When the flow of $\rm H_2O$ was stopped, the $\rm SO_3$ concentration sharply decreased to nearly zero and then returned to a constant of 12 ppm. The sharp decrease in the $\rm SO_3$ concentration occurred because more active sites were released by the $\rm H_2O$ desorption and more $\rm SO_3$ was adsorbed.

The effects of NH_3 on SO_3 formation are shown in Fig. 9. With the addition of NH_3 , the SO_3 concentration slightly increased from 11 ppm to 13 ppm. When the flow of NH_3 was stopped, the SO_3 concentration sharply decreased to 3 ppm and then recovered and remained constant. The desorption of SO_3 was promoted by the competitive adsorption between NH_3 and SO_3 and was inhibited by the combination of SO_3 and adsorbed NH_3 . When NH_3 was initially introduced, competitive adsorption dominated the process, and the release of SO_3 increased slightly. When the NH_3 was withdrawn, the competitive adsorption basically stopped, but the combination of SO_3 and adsorbed NH_3 remained, which greatly inhibited the desorption of SO_3 and led to a sharp drop in the SO_3 concentration.

In short, the process of gaseous SO_3 formation includes SO_2 adsorption, SO_2 oxidation and SO_3 desorption. To clarify in which step NO_x , H_2O and NH_3 affect SO_3 formation, the three steps were tested separately. The SO_2 oxidation was investigated first, followed by the SO_2 adsorption and SO_3 desorption.

3.4. Effects of NO_x, H₂O and NH₃ on SO₂ oxidation

To further investigate the effects of NO_x , H_2O and NH_3 on SO_2 oxidation, *in situ* DRIFT spectroscopy was used to determine the intermediate products, and the results are shown in Fig. 10–12. As shown in Fig. 10, in the presence of NO_x , the adsorption band of N_2O at 1303 cm⁻¹ appeared, ^{36,37} the adsorption band of V=O at 2041 cm⁻¹ decreased, and the peak of tridentate sulfate at 1380–1386 cm⁻¹ decreased. Thus, NO_x was reduced to N_2O while V^{3+} was oxidized to V^{5+} , and the increase in V^{5+} promoted



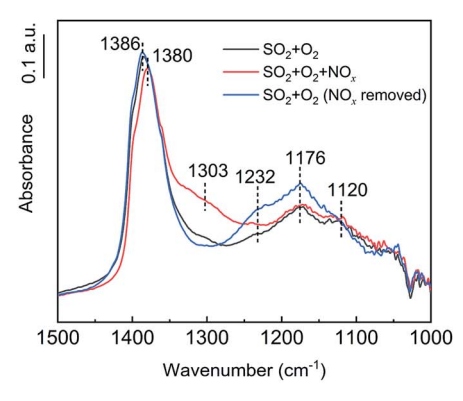


Fig. 10 In situ DRIFT spectra of the catalyst with NO_x flow (conditions: 1000 ppm SO₂, 500 ppm NO_x, 6 vol% O₂, and N₂).

RSC Advances Paper

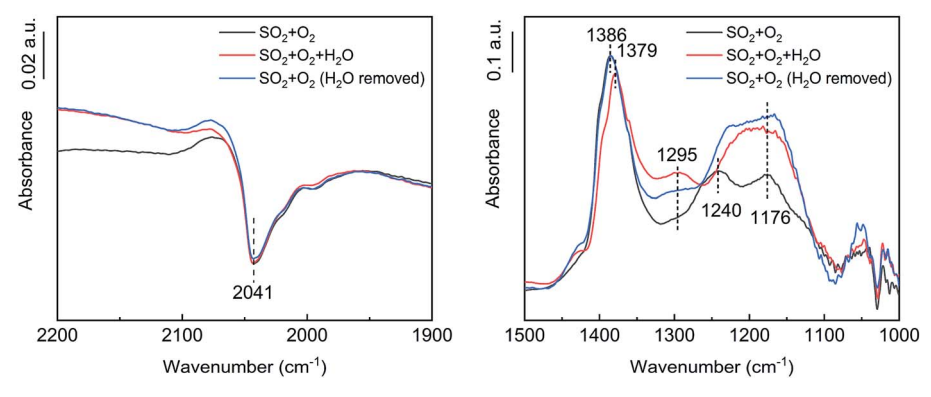


Fig. 11 In situ DRIFT spectra of the catalyst with H₂O flow (conditions: 1000 ppm SO₂, 5 vol% H₂O, 6 vol% O₂, and N₂).

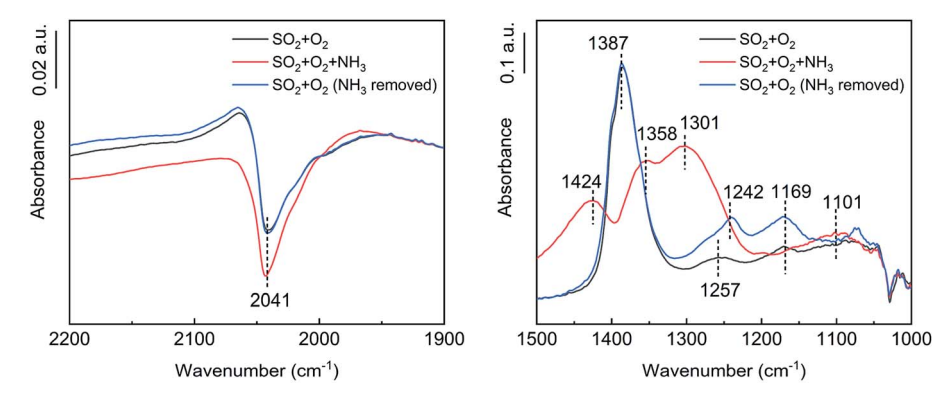


Fig. 12 In situ DRIFT spectra of the catalyst with NH₃ flow (conditions: 1000 ppm SO₂, 500 ppm NH₃, 6 vol% O₂, and N₂).

the oxidation of the adsorbed SO_2 . After the removal of the NO_x , the adsorbed N_2O peak disappeared, and the tridentate sulfate peak returned to its initial state. Therefore, NO_x promoted SO_2 oxidation by promoting the conversion of V^{3+} to V^{5+} . No SO_3 formation was detected in the absence of the catalyst in the SO_2 , O_2 and NO_x atmospheres, indicating that the promotion effect of NO_x on SO_2 oxidation acted on the catalyst surface instead of in the gas phase.

As shown in Fig. 11, after the addition of $\rm H_2O$, the V=O peak at 2041 cm⁻¹ did not change significantly, the tridentate sulfate peak at 1379–1386 cm⁻¹ decreased slightly, and the bidentate sulfate peak at 1176–1240 cm⁻¹ increased. A bending vibration peak attributable to S–O–H was observed at 1295 cm⁻¹, 38 indicating that $\rm H_2O$ promoted the transformation of tridentate sulfate to bidentate sulfate, which partly existed in the form of bisulfate. After the removal of the $\rm H_2O$, the tridentate sulfate peak increased to its initial state, the bidentate sulfate peak increased further, and the bending vibration peak of S–O–H decreased, indicating that the proportion of hydrogen sulfate decreased

As shown in Fig. 12, in the presence of NH_3 , the peak position of tridentate sulfate shifted from 1387 cm⁻¹ to 1588 cm⁻¹, and the peak intensity decreased significantly. Further, new adsorption bands of NH_4^+ at 1424 cm⁻¹ and S-O-H at 1301 cm⁻¹ appeared.³⁹ NH_3 was partially oxidized on the catalyst surface to produce H_2O . In addition, there were hydroxyl groups on the catalyst surface. Thus, tridentate sulfate

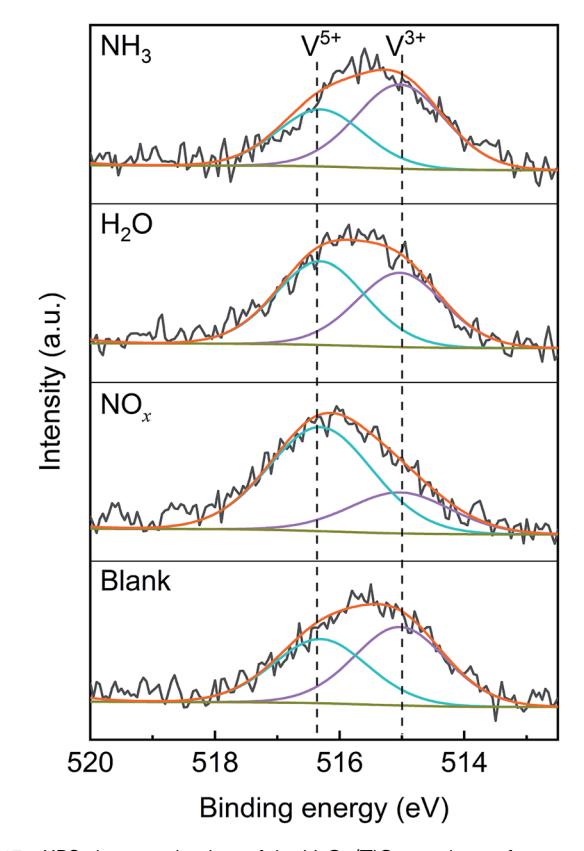


Fig. 13 XPS characterization of the V_2O_5/TiO_2 catalysts after exposure to various gases (blank conditions: 1000 ppm SO_2 and N_2 ; other conditions: addition of 500 ppm NO_x , 500 ppm NH_3 or 5% H_2O).

Table 4 $\,$ XPS analysis for the V_2O_5/TiO_2 catalysts after exposure to various gases

Sample	Blank	NO_x	H_2O	NH_3
$V^{5+}/(V^{5+}+V^{3+})$	46%	72%	53%	40%

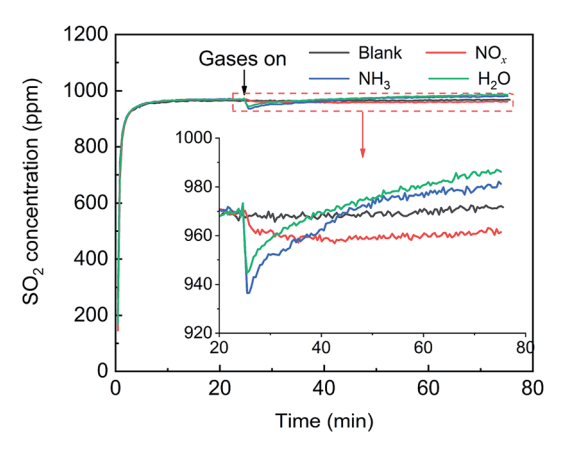


Fig. 14 Effects of NO_x , H_2O and NH_3 on SO_2 adsorption over the V_2O_5/TiO_2 catalyst (blank conditions: 1000 ppm SO_2 and N_2 ; other conditions: 500 ppm NO_x , 500 ppm NH_3 or 5% H_2O).

combined with NH₃ and hydroxyl or H₂O to produce ammonium bisulfate. The adsorption band of V=O increased in the presence of NH₃, showing that V⁵⁺ was reduced to V³⁺ by NH₃. The decrease of V⁵⁺ inhibited the oxidation of the adsorbed SO₂.

To confirm the effects of NO_x, H₂O and NH₃ on the valence state of vanadium, XPS characterization was performed on the V₂O₅/TiO₂ catalysts exposed to various atmospheres, and the spectra are shown in Fig. 13. The V 2p_{3/2} spectra were separated into two peaks by the Gaussian-Lorentzian deconvolution method, including the V³⁺ peak (515.0 eV) and V⁵⁺ peak (516.4 eV),40,41 and the vanadium contents of various valences are shown in Table 4. Compared with the blank catalyst, the proportion of V5+ obviously increased from 46% to 72% in the presence of NOx, which may have been caused by the oxidation of V³⁺ by NO_x. Similarly, the addition of H₂O led to a slight increase in the proportion of V⁵⁺. In contrast, the proportion of V⁵⁺ slightly decreased in the presence of NH₃ because of the reduction of V5+ by NH3. The effect of NOx on the vanadium valence was generally more significant than that of H2O and NH_3 .

Based on the analysis of the results shown in Fig. 10-13, NO_x promoted the conversion of V^{3^+} to V^{5^+} , thereby accelerating the oxidation of the adsorbed SO_2 . The tridentate sulfate peak changed with the atmosphere, while the bidentate sulfate peak always increased, indicating that the bidentate sulfate was more stable than the tridentate sulfate, and the tridentate sulfate may have been the key intermediate product of the SO_2 oxidation. It can be inferred that, in the presence of H_2O or NH_3 , the tridentate sulfate transformed to the more stable bidentate sulfate and thereby inhibited the desorption of SO_3 , which was verified by the TPD tests discussed below.

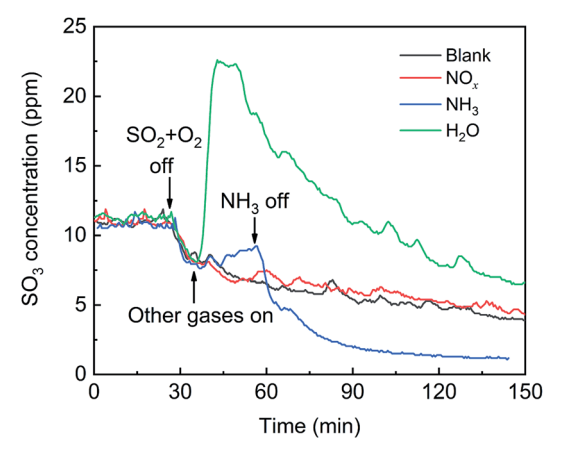


Fig. 15 Effects of NO, H_2O and NH_3 on SO_3 desorption (blank conditions: 1000 ppm SO_2 , 6 vol% O_2 and N_2 ; other conditions: 500 ppm NO, 500 ppm NH_3 or 5% H_2O).

3.5. Effects of NO_x, H₂O and NH₃ on SO₂ adsorption and SO₃ desorption

First, the effects of NO_r, H₂O and NH₃ on SO₂ adsorption were investigated, and the breakthrough curves of SO₂ are shown in Fig. 14. For the blank, the SO₂ concentration increased rapidly, corresponding to the adsorption stage of SO2, and tended to stabilize at 970 ppm, corresponding to the catalytic oxidation stage of SO₂, with a SO₂ conversion ratio of approximately 3%. After the addition of NO_x, the SO₂ concentration decreased from 970 ppm to 960 ppm and tended to be stable, which was attributed to the promotion effect of NO_x on the SO₂ oxidation instead of the SO₂ adsorption. After the addition H₂O or NH₃, the SO₂ concentration rapidly decreased and then gradually increased and finally stabilized at more than 970 ppm. These characteristics are typical of adsorption breakthrough curves, indicating that the presence of H2O or NH3 promoted the SO2 adsorption. Finally, the SO2 concentration exceeded 970 ppm, which was due to the adsorption saturation of the alkaline sites from the adsorption of NH3 and H2O on the catalyst surface.

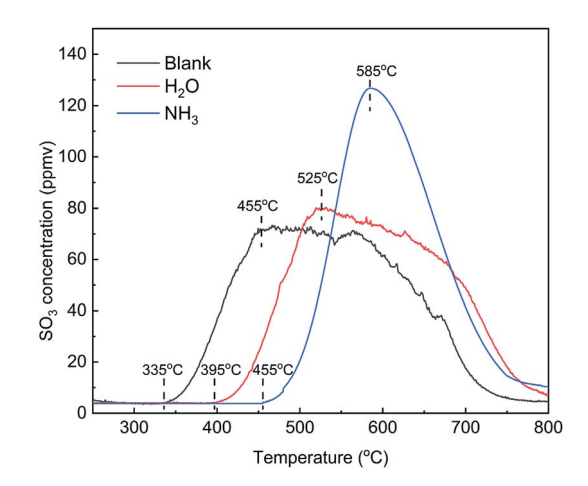


Fig. 16 TPD curves of the catalysts adsorbed in various atmospheres (blank pretreatment conditions: N_2 ; other conditions: 500 ppm NH₃ or 5% H₂O).

RSC Advances

$$\begin{array}{c} \text{H}_2\text{O} / \text{NH}_3 \\ \text{Ti-OH} \\ \text{Ti-OH} \\ \text{Ti-O} \\ \text{Ti-O} \\ \text{Ti-O} \\ \text{V} \\ \text{Ti-O} \\ \text{Ti-O}$$

Formation of SO₃ during the SCR of NO_x with NH₃ in the presence of H₂O₂

The effects of NO_x, H₂O and NH₃ on SO₃ desorption are shown in Fig. 15. For the blank, as the SO₂ and O₂ sources were removed, the SO₃ concentration gradually decreased, showing that the adsorbed SO_3 was desorbed in the flow of N_2 . After the addition of NOx, the desorption curves of SO3 coincided with that of the blank, indicating that NO_x did not influence the SO₃ desorption. After the addition of H₂O, the SO₃ concentration sharply doubled to a maximum and then gradually decreased. These results indicated that there was a strong competitive adsorption between H₂O and SO₃. After the addition of NH₃, the SO₃ concentration gradually increased by approximately 2 ppm due to a mild competitive adsorption between NH₃ and SO₃. H₂O or NH₃ and SO₃ competitively adsorbed to promote SO₃ desorption, but the promotion of SO₃ desorption was not sustainable. Further, H₂O or NH₃ combined with the adsorbed SO₃ to form a more stable bidentate sulfate or ammonium bisulfate, which ultimately inhibited the SO₃ desorption. This phenomenon was most obvious in the presence of NH3. Although the NH3 was removed, the SO3 concentration decreased to less than that of the blank.

The addition of NH₃ and H₂O had an obvious inhibitory effect on the desorption of SO₃. To compare the effects of the two gases, TPD tests were carried out on the catalysts pretreated in various atmospheres, and the results are shown in Fig. 16. Compared with the blank, the initial temperature and peak temperature of SO₃ desorption both increased by 60-70 °C in the presence of H₂O and increased significantly by 120-130 °C in the presence of NH₃. These results showed that the presence of H₂O and NH₃ made SO₃ much more difficult to desorb and that NH3 inhibited SO3 desorption more effectively than did H₂O. The peak areas of SO₃ desorption were 19 615, 20 185 and 21 011 ppm min in three kinds of atmospheres. In view of the measurement error of approximately 10%, the desorption amount of SO₃ was approximately equal. Thus, H₂O and NH₃ affected the adsorption state of SO₃ but not the adsorption amount.

The formation of SO_3 during the SCR of NO_x with NH_3 in the presence of H₂O is summarized in Fig. 17. The formation of SO₃ was obviously promoted by NO_x , significantly inhibited by NH_3 , and slightly inhibited by H₂O. NO_x promoted the SO₂ oxidation in that the NO_r promoted the transformation of low-valent vanadium to high-valent vanadium. H2O and NH3 combined with the adsorbed SO₃ to form bidentate sulfate and bisulfate, respectively, and the SO₃ desorption was depressed. The inhibition of the SO₃ desorption by NH₃ was stronger than that by H₂O.

4. Conclusions

Over the range of conditions studied, the rate of SO₂ oxidation was zero-order in O2, 0.77-order in SO2 and -0.19-order in SO3, and the apparent activation energy for SO₂ oxidation was 74.3 kJ mol⁻¹. The chemical reaction process can be roughly divided into three steps, including (1) SO₂ adsorption on the active site to generate adsorbed SO2, (2) the oxidation of adsorbed SO₂ to produce adsorbed SO₃ in the form of tridentate sulfate and (3) the desorption of SO₃ from the catalyst surface to the gas phase. NO_x promoted the transformation of low-valent vanadium to high-valent vanadium, which promoted SO₂ oxidation and resulted in a significant increase in SO3. However, the presence of NO_x had no obvious effect on the SO₂ adsorption and SO₃ desorption. The presence of H₂O or NH₃ promoted SO₂ adsorption and had no significant effect on SO₂ oxidation. However, H₂O and NH₃ combined with tridentate sulfate to form a more stable bidentate sulfate and ammonium bisulfate, respectively, and SO₃ desorption was depressed. The difference was that the inhibition of SO₃ desorption by NH₃ was more obvious than that by H₂O. Thus, the formation of gaseous SO₃ was significantly inhibited by NH3 and slightly inhibited by H_2O .

Conflicts of interest

There are no conflicts to declare.

Acknowledgements

The authors acknowledge the financial support from the National Key R&D Program of China (No. 2017YFC0210600) and the National Natural Science Foundation of China (No. 21477131).

Paper

References

- 1 R. K. Srivastava, C. A. Miller, C. Erickson and R. Jambhekar, *J. Air Waste Manage. Assoc.*, 2004, 54, 750–762.
- 2 Y. Cao, H. C. Zhou, W. Jiang, C. W. Chen and W. P. Pan, Environ. Sci. Technol., 2010, 44, 3429–3434.
- 3 Y. Sarbassov, L. Duan, V. Manovic and E. J. Anthony, *Greenhouse Gases: Sci. Technol.*, 2018, **8**, 402–428.
- 4 B. Xiang, M. Zhang, Y. Wu, H. Yang, H. Zhang and J. Lu, *Energy Fuels*, 2017, 31, 6284–6297.
- 5 C. H. Weng, D. Yang, Y. Luo, X. Ye, W. Chen, J. Guo, Z. Zou, F. Lu and R. Weerasinghe, *E3S Web Conf.*, 2018, 53, 04005.
- 6 R. Kikuchi, Environ. Manage., 2001, 27, 837-844.
- 7 P. Forzatti, I. Nova and A. Beretta, *Catal. Today*, 2000, 56, 431–441.
- 8 K. He, Q. Song, Z. Yan, N. Zheng and Q. Yao, *Fuel*, 2019, **242**, 355–361.
- 9 D. Xie, H. Wang, J. Tao, D. Chang and C. You, J. Chem. Technol. Biotechnol., 2019, 94, 2382–2388.
- 10 J. Liu, F. Zhu and X. Ma, Engineering, 2018, 4, 416-420.
- 11 S. Meng, X. Qi, W. Yao and Y. Yao, *IOP Conf. Ser. Earth Environ. Sci.*, 2019, **300**, 052018.
- 12 J. P. Dunn, H. G. Stenger and I. E. Wachs, *J. Catal.*, 1999, **181**, 233–243.
- 13 J. P. Dunn, H. G. Stenger and I. E. Wachs, *Catal. Today*, 1999, 53, 543–556.
- 14 J. P. Dunn, H. G. Stenger and I. E. Wachs, *Catal. Today*, 1999, 51, 301–318.
- 15 J. P. Dunn, P. R. Koppula, H. G. Stenger and I. E. Wachs, *Appl. Catal.*, *B*, 1998, **19**, 103–117.
- 16 X. Guo, C. Bartholomew, W. Hecker and L. L. Baxter, *Appl. Catal.*, *B*, 2009, **92**, 30–40.
- 17 L. Lietti, I. Nova, E. Tronconi and P. Forzatti, in *Reaction Engineering for Polution Prevention*, ed. M. A. Abraham and R. P. Hesketh, Elsevier Science, 2000, pp. 85–112.
- 18 E. Tronconi, A. Cavanna, C. Orsenigo and P. Forzatti, *Ind. Eng. Chem. Res.*, 1999, 38, 2593–2598.
- 19 L. Lietti, I. Nova, E. Tronconi and P. Forzatti, *Catal. Today*, 1998, **45**, 85–92.
- 20 C. Orsenigo, A. Beretta, P. Forzatti, J. Svachula, E. Tronconi, F. Bregani and A. Baldacci, *Catal. Today*, 1996, 27, 15–21.
- 21 J. Svachula, L. Alemany, N. Ferlazzo, P. Forzatti, E. Tronconi and F. Bregani, *Ind. Eng. Chem. Res.*, 1994, 33, 1644.

- 22 J. Svachula, L. J. Alemany, N. Ferlazzo, P. Forzatti, E. Tronconi and F. Bregani, *Ind. Eng. Chem. Res.*, 1993, 32, 826–834.
- 23 J. Xiong, Y. Li, J. Wang, Y. Yang and T. Zhu, J. Environ. Sci., 2018, 72, 25–32.
- 24 D. Yun, Y. Wang and J. E. Herrera, ACS Catal., 2018, 8, 4681–4693.
- 25 S. Najafishirtari, C. Guglieri, S. Marras, A. Scarpellini, R. Brescia, M. Prato, G. Righi, A. Franchini, R. Magri, L. Manna and M. Colombo, *Appl. Catal.*, B, 2018, 237, 753–762.
- 26 J. Mu, X. Li, W. Sun, S. Fan, X. Wang, L. Wang, M. Qin, G. Gan, Z. Yin and D. Zhang, *Ind. Eng. Chem. Res.*, 2018, 57, 10159–10169.
- 27 S. T. Choo, Y. G. Lee, I.-S. Nam, S.-W. Ham and J.-B. Lee, Appl. Catal., A, 2000, 200, 177–188.
- 28 C. E. Nanayakkara, J. Pettibone and V. H. Grassian, *Phys. Chem. Chem. Phys.*, 2012, 14, 6957–6966.
- 29 C. E. Nanayakkara, W. A. Larish and V. H. Grassian, J. Phys. Chem. C, 2014, 118, 23011–23021.
- 30 U. Diebold, Surf. Sci. Rep., 2003, 48, 53-229.
- 31 J. Ryczkowski, Catal. Today, 2001, 68, 263-381.
- 32 S. M. Jung, O. Dupont and P. Grange, *Appl. Catal.*, *A*, 2001, **208**, 393–401.
- 33 C. Li, M. Shen, T. Yu, J. Wang, J. Wang and Y. Zhai, *Phys. Chem. Chem. Phys.*, 2017, **19**, 15194–15206.
- 34 K. Nakamoto, Infrared and Raman Spectra of Inorganic and Coordination Compounds (Part B: Applications in Coordination, Organometallic, and Bioinorganic Chemistry), John Wiley & Sons, Inc., Hoboken, New Jersey, 2009, vol. 1B.
- 35 A. Marberger, D. Ferri, M. Elsener and O. Krocher, *Angew. Chem., Int. Ed.*, 2016, 55, 11989–11994.
- 36 K. I. Hadjiivanov, Catal. Rev., 2000, 42, 71-144.
- 37 T. M. Miller and V. H. Grassian, *J. Am. Chem. Soc.*, 1995, **117**, 10969–10975.
- 38 A. Periasamy, S. Muruganand and M. Palaniswamy, *Rasayan J. Chem.*, 2009, **2**(4), 981–989.
- 39 F. Liu, K. Asakura, H. He, W. Shan, X. Shi and C. Zhang, *Appl. Catal.*, *B*, 2011, **103**, 369–377.
- 40 Q. Wang and R. J. Madix, Surf. Sci., 2001, 474, L213-L216.
- 41 M. A. Eberhardt, A. Proctor, M. Houalla and D. M. Hercules, *J. Catal.*, 1996, **160**, 27–34.